



**HAL**  
open science

## Optimised chaotic mixer configurations for process industries: a numerical study

Akram Ghanem, Thierry Lemenand, Dominique Della Valle, Hassan Peerhossaini

► **To cite this version:**

Akram Ghanem, Thierry Lemenand, Dominique Della Valle, Hassan Peerhossaini. Optimised chaotic mixer configurations for process industries: a numerical study. ASME- FEDSM 2013, 2013, Nevada, United States. pp.10. hal-03287154

**HAL Id: hal-03287154**

**<https://univ-angers.hal.science/hal-03287154>**

Submitted on 15 Jul 2021

**HAL** is a multi-disciplinary open access archive for the deposit and dissemination of scientific research documents, whether they are published or not. The documents may come from teaching and research institutions in France or abroad, or from public or private research centers.

L'archive ouverte pluridisciplinaire **HAL**, est destinée au dépôt et à la diffusion de documents scientifiques de niveau recherche, publiés ou non, émanant des établissements d'enseignement et de recherche français ou étrangers, des laboratoires publics ou privés.

FEDSM-16115

## OPTIMIZED CHAOTIC HEAT EXCHANGER CONFIGURATIONS FOR PROCESS INDUSTRY: A NUMERICAL STUDY

**Akram Ghanem**

LUNAM Université, Laboratoire de Thermocinétique de  
Nantes, CNRS UMR 6607, 44306 Nantes, France

**Dominique Della Valle**

ONIRIS – Nantes  
44322 Nantes, France

**Thierry Lemenand**

LUNAM Université, Laboratoire de Thermocinétique de  
Nantes, CNRS UMR 6607, 44306 Nantes, France

**Hassan Peerhossaini**

Univ. Paris Diderot, Sorbonne Paris Cité, Institut des  
Energies de Demain (IED), 75013 Paris, France

### ABSTRACT

A numerical investigation of chaotic laminar flow and heat transfer in isothermal-wall square-channel configurations is presented. The computations, based on a finite-volume method with the SIMPLEC algorithm, are conducted in terms of Péclet numbers ranging from 7 to  $7 \times 10^5$ . The geometries, based on the split-and-recombine (SAR) principle, are first proposed for micromixing purposes, and are then optimized and scaled up to three-dimensional minichannels with 3-mm sides that are capable of handling industrial fluid manipulation processes. The aim is to assess the feasibility of this mass- and heat-transfer technique for out-of-laboratory commercial applications and to compare different configurations from a process intensification point of view. The effects of the geometry on heat transfer and flow characteristics are examined. Results show that the flux recombination phenomenon mimicking the baker's transform in the SAR-1 and SAR-2 configurations produces chaotic structures and promotes mass transfer. This phenomenon also accounts for higher convective heat transfer exemplified by increased values of the Nusselt number compared to the chaotic continuous-flow configuration and the baseline plain square-duct geometry. Energy expenditures are explored and the overall heat transfer enhancement factor for equal pumping power is calculated. The SAR-2 configuration reveals superior heat-transfer characteristics, enhancing the global gain by up to 17-fold over the plain duct heat exchanger.

### KEYWORDS

Process intensification; mass and heat transfer enhancement; chaotic advection; square channel; Split-And-Recombine heat exchanger/reactor

### NOMENCLATURE

$D_h$	channel hydraulic diameter (m)
$f$	friction factor
$h$	convective heat-transfer coefficient ( $\text{W m}^{-2} \text{K}^{-1}$ )
$L$	channel developed length (m)
$n$	number of splitting and recombination (SAR) steps
$Nu$	Nusselt number
$P$	Pressure (Pa)
$Pe$	Péclet number
$Pr$	Prandtl number
$Re$	Reynolds number
$T$	temperature (K)
$u$	local velocity ( $\text{m s}^{-1}$ )
$\bar{u}$	volume-averaged velocity ( $\text{m s}^{-1}$ )
$U$	inlet velocity ( $\text{m s}^{-1}$ )

#### Greek symbols

$\alpha$	fluid thermal diffusivity ( $\text{m}^2 \text{s}^{-1}$ )
$\eta$	thermal enhancement factor
$\kappa$	fluid thermal conductivity ( $\text{W m}^{-1} \text{K}^{-1}$ )
$\rho$	fluid density ( $\text{kg m}^{-3}$ )
$\varphi$	heat flux density ( $\text{W m}^{-2}$ )
$\mu$	fluid dynamic viscosity (Pa s)
$\Delta P$	pressure drop (Pa)

#### Subscripts

$0$	plain channel
$b$	bulk value
$x$	local value
$w$	wall

## INTRODUCTION

With increasing demand for energy efficiency and compact process inventory for industrial applications, many engineering techniques have been devised over the last decades to improve mixing and convective heat-transfer rates in the category of devices called multifunctional heat exchangers/reactors, which are capable of handling processes in which mass and heat transfer are strongly coupled.

Artificial vortex generation using flow perturbators is an efficient technique extensively studied and widely used in static mixers and heat exchangers operating in the inertial or slightly turbulent regimes [1-5]. The vortical structures created downstream of vortex generators, like the trapezoidal tabs in the high-efficiency vortex (HEV) heat exchanger and static mixer, induce transverse fluid particle transport, inhibit the development of hydrodynamic and thermal boundary layers, and produce transfer rates comparable to highly turbulent flows with only moderate pressure losses [6-8]. Another technique is to produce swirl flow using helical inserts in tubular heat exchangers. Fluid particles are entrained by the swirling motion and are forced to visit various cross-sectional locations, increasing fluid-fluid interaction and promoting transport between the wall region and the core flow [9]. Other types of inserts have been recently developed, some producing complex flow structures that enhance transport further, like the Helical Kenics mixer and heat exchanger [10]. Annular vortices produced by laminar or turbulent jets are also known to enhance surface heat transfer by breaking the thermal boundary layer [11]. Surface curvature, as in helical tubes or corrugated channels, where the imbalance between centrifugal and inertial forces produces such transverse secondary flows and longitudinal vortices as Dean and Görtler instabilities, has also been found to be effective in mass- and heat-transfer augmentation [12-13].

The interest of the above techniques is that they exploit the flow energy to induce beneficial structural modifications without requiring costly active control methods like agitation, stirring, or mobile surfaces. However, in some cases when the flow is deeply laminar or the device dimensions are small, the creation of vortical structures becomes difficult and the incorporation of inserts or turbulators becomes technically complicated and energetically costly. Chaotic advection in creeping flows induced by modified geometries (usually periodic wall curvatures) is one of the most efficient passive mass- and heat-transfer enhancement methods in systems where deep flow laminarity prevents the creation of artificial turbulent structures [12,14,15]. This phenomenon, by virtue of which the laminar fluid strata are broken and fluid particles follow complex trajectories along the entire channel cross-section, has been widely studied and found feasible in many mixing and heat-transfer applications [16,17,18].

Another approach to transport enhancement in laminar flows is a direct contribution of mathematics to conservative

dynamical systems and consequently to fluid flow: the baker's map [19-21] defined on the unit square by

$$S(x, y) = \begin{cases} (2x, \frac{1}{2}y) \bmod 1, & \text{if } 0 \leq x < \frac{1}{2} \\ (2x, \frac{1}{2}(y+1)) \bmod 1, & \text{if } \frac{1}{2} \leq x < 1 \end{cases} \quad (1)$$

Figure 1 shows two iterations of the transformation  $S$  on the unit square. The upper and lower halves are mapped when the transformation  $S$  is repeatedly applied. Squeezing along  $y$  while stretching along  $x$ , cutting in two and then stacking the right half above the left, causes the two-strip domain to become  $2^{n+1}$  strips after  $n$  iterations. The baker's map is a mixing transformation since, for a large number of iterations, the unit square becomes completely filled with an infinite number of alternating black and green lines of decreasing thickness after each iteration, so that any infinitesimal region of the square contains the same proportion of the two colors. In addition to the contribution to mixing, heat transfer is substantially enhanced by the increased contact area between different fluid strips. Fluid particles heated by the wall flux eventually migrate to the core region as the flow is cut and stacked, transporting energy to colder fluid parcels.

The split-and-recombine (SAR) heat exchangers and passive static mixers, subjects of the present study (Fig. 2), join the effects of flow splitting and recombination, where the chaotic nature is conveyed by the exponential increase in interfacial area between flow lamellae, to those of curved walls where chaotic advection is produced by virtue of abrupt changes in flow direction. They have been recently investigated by experimental and numerical means [22-27], but most of the studies examined mixing rather than heat transfer and usually on microscales. The main aim of the present work is to characterize the nature of heat transfer in these devices, assess the feasibility of their use in process industries on a relatively larger scale, and compare the performance of various configurations. The following section describes the configurations studied and introduces the hydrodynamic and thermal parameters of the imposed flow. Subsequently, the mathematical background for the numerical solution together with the pertinent physical parameters and boundary conditions are presented. The validation of the model and the hydrodynamic and thermal results are then discussed. Finally, some conclusions are drawn on the feasibility and interest of using SAR devices in process industries.

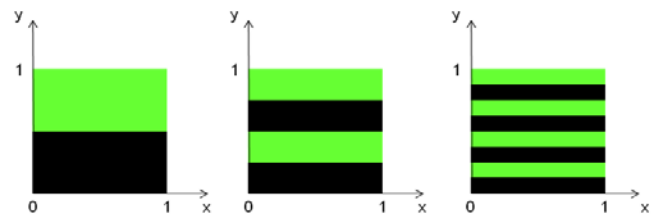


FIG. 1. BAKER'S TRANSFORM APPLIED TO THE UNIT SQUARE

## GEOMETRY AND FLOW

Figure 2 shows the elementary structural units of the SAR configurations studied, SAR-1 and SAR-2, together with that of a continuous three-dimensional chaotic flow duct, referred to hereafter as 3D-Flow. This last serves to isolate the effect of splitting and recombination on heat transfer from that of the surface curvature. Results are normalized by the values obtained in a plain square duct serving as a baseline geometry.

The configurations, called SAR-1 and SAR-2 for the number of splits and recombinations in the elementary unit, were first proposed on a microscale by Gray *et al.* [22] and Chen and Meiners [23] respectively. The network of separated and then recombined channels creates chaotic trajectories in a laminar flow. They present topological structures that exploit the flow laminarity repeatedly to fold the fluid layers and double the lateral concentration gradient, thus providing fast mixing by diffusion in a compact geometry. This topology performs a series of baker's transforms on the concentration profile. The fluid streams are combined split out of plane, rotated in opposite directions, and recombined, folding over the concentration profile and doubling the lateral gradient. Successive vertical separation and horizontal reuniting of fluid streams increase the number of laminates with each stage, rapidly increasing the contact area between the two fluids to produce faster mixing. Recent investigations by Carrière [24] reveal the chaotic nature of the SAR flow and under favorable conditions, the maximum value of the Lyapunov exponent  $\ln(2)$  was recorded in SAR-1.

Complex interactions between chaotic advection and diffusion yield enhanced dispersion [28]. Mixing and heat transfer are enhanced without generating prohibitive losses while maintaining a sufficient residence time for reactive flows [29]. This type of device is especially interesting in the petrochemical, pharmaceutical, or food industries, which frequently handle viscous and fragile fluids. Mixing and heat transfer can be accomplished without generating prohibitive losses or excessive shear that might in some cases alter the rheological nature of the sensitive non-Newtonian products used in these industries [30-31].

In the present work, the configurations are optimized in terms of the total developed length, the hydraulic diameter, and the ratio of the linear distances traveled by the fluid particles before encountering a singularity to the channel hydraulic diameter. The SAR-1, SAR-2, and 3D-Flow configurations are respectively made up of 13, 10, and 18 elementary units (Fig. 2). The number of units per exchanger is chosen so that all configurations have the same residence time, given the importance of this parameter for both reactive flows and diffusive heat transfer. The corresponding length of the plain duct is 750 mm with an equal hydraulic diameter  $D_h = 3$  mm. Each heat exchanger is equipped at its inlet with a pre-conditioner 10 diameters in length (30 mm) in order to ensure a fully developed flow at the inlet of the test section. Downstream from the last element outlet, the geometry also

incorporates a post-conditioner to damp any effects of the external conditions on the calculated parameters.

Reynolds numbers are calculated based on the hydraulic diameter and the inlet flow velocities. The working fluid viscosity is chosen to match that of viscous fluid products encountered in industrial applications where SAR devices are suitable. A fixed dynamic viscosity of 10 Pa s is used for the flow simulations. The other fluid physical properties are the same as those of water at 300 K. The corresponding Prandtl number is kept constant at  $697 \times 10^2$ . The control parameter is the Péclet number  $Pe$  describing the ratio of advection to diffusion, which gives interesting insight into the physical phenomena taking place in such flows. The range of Péclet numbers studied is between 7 and  $7 \times 10^5$  and the corresponding Reynolds number varies between  $10^{-4}$  and  $10^1$  giving a Brinkman number variation between  $3 \times 10^{-8}$  and  $3 \times 10^2$  and thus covering a wide range of possible operating conditions.

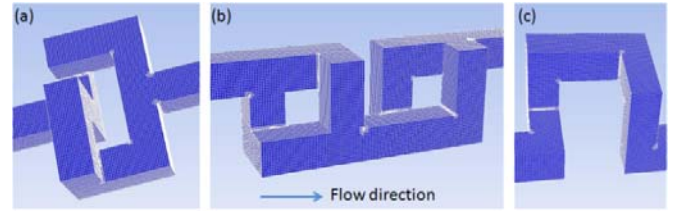


FIG. 2. ELEMENTARY UNITS OF CONFIGURATIONS STUDIED: (a) SAR-1, (b) SAR-2, (c) 3D-FLOW

## MODELING AND NUMERICAL SIMULATION

### Mathematical foundation

The numerical model for fluid flow and heat transfer in the square ducts is developed under the following assumptions:

- Steady three-dimensional fluid flow and heat transfer
- Laminar and incompressible flow
- Constant fluid properties
- Negligible radiation heat transfer
- Body forces and viscous dissipation ignored

Based on the above assumptions, the duct flow is governed by the continuity, the momentum, and the energy equations. In the Cartesian tensor system, after simplification, these equations can be respectively written as follows:

$$\frac{\partial}{\partial x_i}(\rho u_i) = 0 \quad (2)$$

$$\frac{\partial}{\partial x_j}(\rho u_i u_j) = -\frac{\partial P}{\partial x_i} + \frac{\partial}{\partial x_j} \left[ \mu \left( \frac{\partial u_i}{\partial x_j} + \frac{\partial u_j}{\partial x_i} \right) \right] \quad (3)$$

$$\frac{\partial(\rho u_i T)}{\partial x_i} = \frac{\partial}{\partial x_j} \left( \frac{\mu}{Pr} \frac{\partial T}{\partial x_j} \right) \quad (4)$$

## Numerical procedure

The solver used for the flow computation is the CFD code FLUENT<sup>®</sup> installed on a 64-bit double-core 2.67 GHz Intel Xenon processor with 12 GB of RAM. The computational mesh is a cell-centered finite-volume discretization. The solver is a double-precision, segregated, steady, implicit linearization finite-volume solver. Using the segregated approach, the governing equations are solved sequentially. Quantities at the cell faces are computed using a multidimensional linear reconstruction approach [32-33] to obtain second-order accuracy. Pressure-velocity coupling is achieved by the Semi-Implicit Method for Pressure-Linked Equations — Consistent (SIMPLEC) algorithm, an efficient variant of the SIMPLE algorithm [34] that reduces calculation time and preserves accuracy for laminar flows. Spatial discretization schemes are second order upwind [32] for momentum and PRESTO staggered-variable arrangement for pressure to ensure a maximum accuracy for the cell-face pressure calculation in the strongly curved domains. The GAMBIT software is used to generate the uniform structured mesh initially refined at all solid boundaries with a volume that grows gradually away from the wall. Subsequent adaptations of the grid are carried out in the CFD solver software based on temperature and pressure gradients after a preliminary convergence.

After a series of tests on periodic computational domains corresponding to the elementary SAR units, the solutions are considered to be converged when the normalized residual values are less than  $10^{-7}$  for all variables and less than  $10^{-10}$  for the energy equation. Beyond these values, no significant changes are observed in the velocity or pressure fields, nor in temperature and heat flux distribution.

To test the sensitivity of computed results to grid size, the solver is run for several initial mesh densities. Grids are subsequently adapted after convergence by limiting the maximum temperature and pressure gradients between neighboring cells. Non-uniform grids that are denser in the radial and tangential directions are also tested. Based on a compromise between accuracy and calculation time, the grid chosen contained around  $10^6$  cells resulting from the adaptation of a uniform initial mesh made of 200  $\mu\text{m}$ -side cubic cells. The necessary calculation time for a single simulation using the processor mentioned above is around 18 hours for the SAR configurations for the lower Péclet numbers and up to 22 hours for the higher ones.

## Pertinent parameters

The parameters of interest in the present study are the Reynolds number  $Re$ , the Péclet number  $Pe$ , the convective heat transfer coefficient  $h$ , the Nusselt number  $Nu$ , the friction factor  $f$ , and the thermal enhancement factor  $\eta$ .  $Re$  and  $Pe$  are calculated using the inlet fluid velocity and are respectively defined as:

$$Re = \frac{\rho U D_h}{\mu} \quad (5)$$

$$Pe = \frac{U D_h}{\alpha} \quad (6)$$

The local convective heat-transfer coefficients are calculated using the computed local heat-flux densities and temperature gradients:

$$h_x = \frac{\phi_x}{(T_w - T_b)_x} \quad (7)$$

The local Nusselt numbers characterizing convective heat transfer can be written as:

$$Nu_x = \frac{h_x D_h}{\kappa} \quad (8)$$

The global area-averaged Nusselt numbers can be obtained by:

$$Nu = \frac{1}{A} \int Nu_x \partial A \quad (9)$$

The friction factor is computed from the pressure drop across the developed length of the minichannels as:

$$f = \frac{(\Delta P / L) D_h}{\frac{1}{2} \rho \bar{u}^2} \quad (10)$$

The thermal enhancement factor  $\eta$  is defined as the ratio of the surface heat transfer coefficient in the modified geometry  $h$  to that of a plain surface  $h_0$  at equal pumping power ( $pp$ ) and is given by:

$$\eta = \frac{h}{h_0} \Bigg|_{pp} = \frac{Nu}{Nu_0} \Bigg|_{pp} = \frac{Nu/Nu_0}{\left(\frac{f}{f_0}\right)^{1/3}} \quad (11)$$

## Boundary conditions

In the entrance region, a uniform fluid velocity  $U$  is introduced, while a pressure outlet condition is applied at the exit. The fluid enters the inlet at a temperature of 300 K and is assumed to preserve constant physical properties throughout the test section. It is heated by virtue of the temperature gradient with the wall that is maintained at a constant temperature of 360 K. Impermeable boundary and no-slip wall conditions are implemented over the duct walls. The zero value of the pressure is a reference point for the pressure gradient integration. For other variables, fluxes are set to zero.

## RESULTS AND DISCUSSION

In this section, the validity of the numerical model is discussed and the results are reported for different Péclet numbers in terms of local and global Nusselt numbers, friction

factor and thermal performance in the SAR and 3D-Flow configurations normalized by the values obtained in the plain square duct.

### Model validation

To validate the accuracy of the numerical solutions, computations of fully developed laminar forced convection are carried out in a plain square duct as well as in a circular pipe by adopting the same algorithms and schemes used for the chaotic configurations. The numerical results are compared to exact solutions obtained from the literature [35] and plotted in Fig. 3. The present smooth-channel results are in good agreement with the literature values for both the Nusselt number and the friction factor, with maximum deviations of 1.5% and 1.2% respectively. This gives strong confidence in further investigation of the duct flow in the more complex configurations. The exact solutions of the Nusselt number and the friction factor for laminar flows in square ducts with constant wall temperature are [35]:

$$Nu_0 = 2.98 \quad (12)$$

$$f_0 = 56.92 / Re \quad (13)$$

Thus, the numerical results for the chaotic configurations studied are normalized by the exact solutions of the Nusselt number and the friction factor in Eqs. (12) and (13).

### Flow structure and chaotic behavior

The flow laminarity in the square ducts is imprinted on the general behavior of the velocity field. A global look at the interior of the four configurations conveys a uniform velocity distribution across the entire length that abides by the classical laws of laminar flows. After the inlet length of 10 diameters, a parabolic velocity profile is established in the cross section and is slightly disturbed by the flow curvature. Figure 4(a) shows the streamlines in the SAR-1 configuration for  $Pe = 7000$  colored by the velocity magnitude. Looking at the entire set of pathlines, it is evident that little transverse activity is produced: the fluid seems to follow the channel walls in a parallel motion and the only significant variation is the doubling of the velocity as the split streams are recombined, creating higher flow inertia in the sections connecting two consecutive SAR units. Low-velocity stagnation zones prevail around the corners of the concave outer walls of the three configurations (Fig. 5(a)). On the other hand, the convex corners contribute to rupture of the hydrodynamic boundary layer on the adjacent walls, and the local axial velocity magnitude is consequently higher yet with no significant deformation of the fluid trajectories and the velocity vectors. The latter remain parallel in the axial direction with smooth direction changes at the splits, recombinations and bends, as shown in Fig. 4(b).

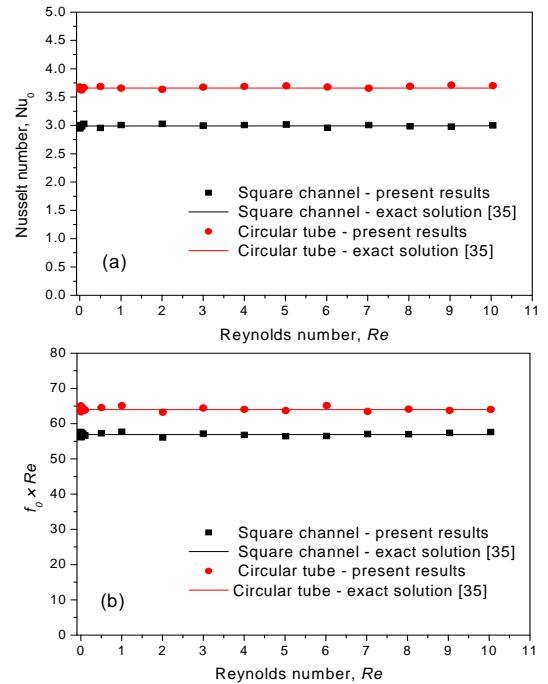


FIG. 3. VALIDATION OF (a)  $Nu_0$  AND (b)  $f_0 \times Re$  FOR PLAIN CHANNELS

In the sections following a recombination, the velocity values double due to the recombination of the two incoming streams with equal flow rates in a constant cross-section channel.

Following the same reasoning, for the same inlet Reynolds number, higher global velocities prevail in the 3D-Flow configuration where no splitting takes place. For an inlet-based Reynolds number  $Re$  in the 3D-Flow configuration, the corresponding volume-averaged Reynolds numbers in SAR-1 and SAR-2 would be  $0.58Re$  and  $0.61Re$  respectively, due to purely geometrical considerations. For a higher range of Reynolds numbers than those studied here, the values of the Dean number are expected to exceed the threshold for secondary Dean flow in the form of counter-rotating cells in the channel cross section. This flow is produced in bent tubes by the imbalance between the viscous inertial forces and the centrifugal forces and is accentuated by the surface curvature even if the flow is laminar [36]. However, in the present case, the flow is of the creeping type and, despite the sharp bends, the Dean numbers remain low due to the small Reynolds numbers and reduced flow inertia given the high viscosity of the working fluid. Consequently, the contribution of the bends to the deformation of the velocity field in the cross section remains limited. Nevertheless, their effect on interrupting the development of the hydrodynamic and thermal boundary layers cannot be neglected and by virtue of this phenomenon, together with the projection of fluid particles onto the hot walls of the bends, the effect of the bends is more clearly seen on the heat transfer rates discussed below.

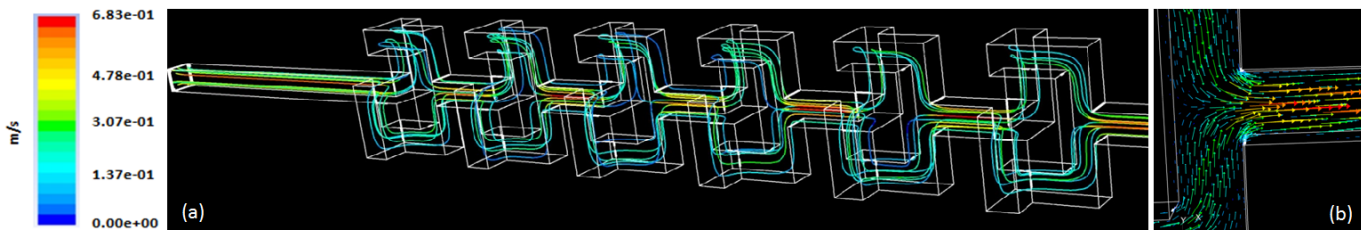


FIG. 4 (a) STREAMLINES OF FLUID PARTICLES COLORED BY VELOCITY MAGNITUDE, (b) VELOCITY VECTORS IN THE SAR-1 CONFIGURATION FOR  $Pe = 7000$ ,  $Re = 0.1$

Nevertheless, the major influence of the SAR configurations on the flow can be unveiled only by scrutinizing the individual particle trajectories, since the particular interest in this case is the production of chaotic structures that create embedded mass transport within the channel cross-section that does not leave a signature on the macroscale velocity field, yet substantially enhances mass transfer and all scalars transportable by fluid particles. In an attempt to reveal the chaotic nature of the SAR flow, one of its fundamental features is explored: its sensitivity to initial conditions. One of the inherent characteristics of chaos is the exponential temporal and spatial deviation of field properties from infinitely close initial points.

Two fluid particles of diameter  $10^{-10}$  m initially separated by the very small distance of  $10^{-9}$  m are released from exactly the same arbitrary position at the inlet section of the four configurations. The corresponding trajectories are depicted in Fig. 6. It is evident from this figure that, in confined zones, separation of the fluid particles is prevented by the channel walls and the chaotic nature is rather periodic. In fact, the spatial chaos cannot be characterized merely by examining the exit locations of the fluid particles.

In Fig. 6(a), the divergence of fluid particle trajectories is detected starting from the 7th SAR unit. In the 8th, the particles are sufficiently far apart but remain in the same fluid stream after the split and traverse the same branch. In the 9th, the trajectories are completely independent: each fluid particle follows a different branch and the maximum deviation is achieved. The next recombination downstream regroups the fluid particles until the state of maximum deviation is reached in the 13th element. The same chaotic behavior is displayed in the SAR-2 configuration (Fig. 6(b)) and the divergence also starts in the 7th element.

For this small initial distance between injected fluid particles, the number of units in the 3D-Flow configuration is not enough to show the chaotic nature induced by the surface curvature (Fig. 6(c)). The chaos ‘intensity’ is higher in the SAR configurations due to the combined effect of the bends and the cutting/stacking mechanism. Nonetheless, it should be noted that increasing the initial distance between the released particles to  $10^{-8}$  m produces, in 3D-Flow, the same chaotic effect seen in the SAR configurations for a distance of  $10^{-9}$  m, and divergence is detected starting at the 8th element. For this

initial distance, divergence in SAR-1 and SAR-2 starts in the 4th element. On the other hand, the particles in the plain duct of Fig. 6(d) conserve exactly the same mutual distance throughout the entire exchanger length, no matter how much the initial releasing distance is increased. They exit the test section at a point having the same radial and tangential coordinates as the releasing point due to the parallel streamlines in laminar flow and the limited transverse activity.

### Convective heat transfer

Mass and heat transfer are closely related phenomena here since heat energy transmitted through the wall by pure conduction is then transported by fluid particles through convection and diffusion. Consequently, the passive influence of the geometry on flow hydrodynamics is directly reflected in the thermal behavior of the flow. Close inspection of Figs. 7(a) and 7(b) reveals the link between the velocity and the temperature fields, in addition to the imprints of the SAR mechanism on the heat-transfer map in the chaotic exchanger. The low-velocity zones around the concave corners of the bends exhibit poor heat evacuation from the wall region to the core flow, and local overheated fluid zones are produced where convective heat transfer is weak.

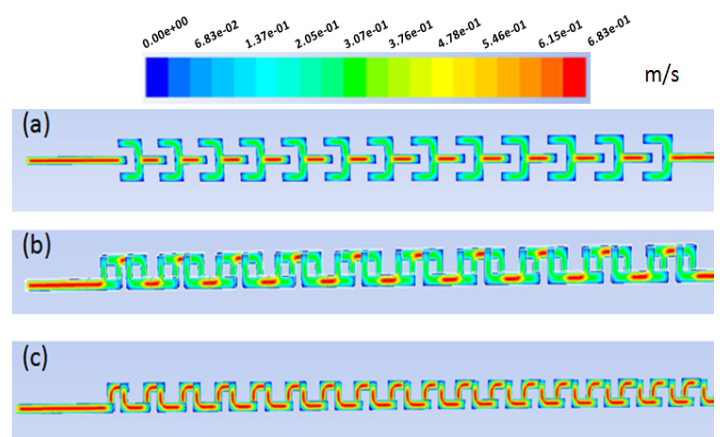
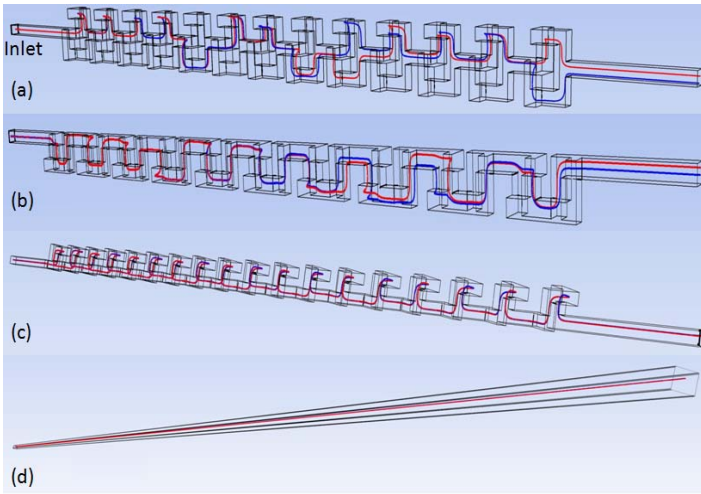


FIG. 5 VELOCITY CONTOURS FOR  $Pe = 7000$ ,  $Re = 0.1$  IN (a) SAR-1, (b) SAR-2 AND (c) 3D-FLOW



**FIG. 6 TRAJECTORY EVOLUTION OF TWO INITIALLY INFINITELY CLOSE PARTICLES FOR  $Pe = 7000$ ,  $Re = 0.1$  IN (a) SAR-1, (b) SAR-2, (c) 3D-FLOW, AND (d) SQUARE DUCT**

On the other hand, the temperatures of the colder zones around the convex corners can be matched with the higher flow velocities in these regions after the breakage of the hydrodynamic boundary layer accompanied by an abrupt increase in the local heat-transfer rate in the direct vicinity of the bend. A close look at the temperature contours in the linear section between the first two elements shows the presence of a hot strip in the flow core between two colder zones from above and below. In conventional heat-transfer devices, the core flow is the coldest region because it is the farthest from the walls. Here, the hot zone is the signature of the SAR mechanism. As the fluid streams are cut, squeezed, stretched, turned, and stacked, the strips near the wall end up in the middle of the pile right after the converging zone of the SAR unit. This hot core becomes less distinct as the flow advances since multiple hot strips are produced after each step and the increased interfacial area helps to homogenize the temperature gradients through diffusion, contributing to the overall heat-transfer enhancement.

It should also be noted that in the direct vicinity of the diverging zone where fluid streams are split, a sharp increase in the surface heat flux is recorded in both SAR configurations. Also, since the local bulk temperatures in these zones encounter no sudden changes compared to the surrounding fluid, the local Nusselt numbers downstream from the splitting zones exhibit sharp peaks visible in Fig. 8. In this figure, the relative local Nusselt numbers over the heat exchanger length are plotted against the normalized axial coordinates starting from the pre-conditioner outlet. Each value of  $Nu_x$  on this plot represents the average of the solutions obtained in the grid cells sharing the same axial position. The peaks can be explained by the improved transverse mass transport as fluid particles of a half-stream upstream of the split ‘rush’ sideways and expand to fill up the entire section downstream. The amplitude of these peaks can reach a maximum of 3.2 times greater than the mean in

SAR-2 and up to 3.8 times in SAR-1 because, in the SAR-1 design, splitting occurs in a topological diverging T and the streams are forced to leave the middle plane directly after encountering a solid wall that hinders the axial flow. The incoming fluid impinges on this wall and causes a boost in heat transfer that is absent from SAR-2 owing to the different design in which only one of the fluid streams changes flow plane after each split. The high values of Nusselt number prevail over a length of one diameter before becoming rapidly attenuated by the rearrangement of the viscous fluid strata, and the average transfer rates reappear in the linear sections of the geometry. These high-amplitude peaks are naturally absent from the 3D-Flow configuration where no splitting occurs, although this configuration exhibits smaller-amplitude peaks with maximum value 2.1 times higher than the mean. This is the signature of the boundary layer destruction and possible instabilities at the convex corners of the sharp bends.

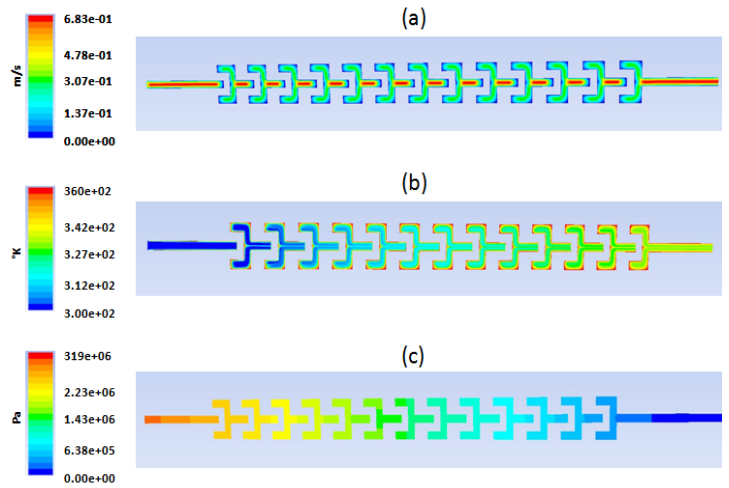


**FIG. 7 CONTOURS OF (a) VELOCITY, (b) TEMPERATURE AND (c) STATIC PRESSURE FOR  $Pe = 7000$ ,  $Re = 0.1$ ,  $Pr = 69700$  IN THE MEDIAN PLANE OF SAR-1**

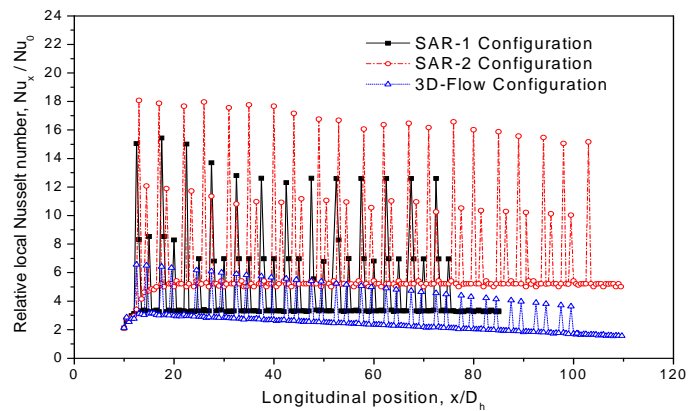


**FIG. 8 LONGITUDINAL VARIATION OF RELATIVE LOCAL NUSSLETT NUMBER**

This phenomenon is also seen in the two other configurations that also exhibit abrupt modifications of flow direction and is conveyed by the shorter apices of the plot in Fig. 8; the ratio to the mean is almost equal in the three geometries. At the inlet of the arrays, for a value of  $x/D_h = 10$ , the three exchangers exhibit the same heat-transfer rate before the intervention of the first units. The Nusselt numbers then rapidly increase and stabilize over a distance of 10 hydraulic diameters; beyond this, little variation can be seen except for a general decreasing tendency that is more visible in the peaks of the SAR configurations that conserve an almost constant mean value across the exchanger length. On the other hand, the 3D-Flow configuration behaves similarly to a plain channel: the mean value of the Nusselt number decreases with the axial distance from the inlet. Owing to their unique periodic mechanism, the flow in the SAR configurations is continuously regenerated and they are able to inject or evacuate heat with longitudinally homogeneous transfer rates.

Conventionally, one might expect that in the connecting sections between two consecutive SAR units, the increased local velocity would favor the local convective transfer over the other zones. Yet this is not confirmed by the numerical study, suggesting that the nature of the enhancement in these configurations, for the range of  $Re$  and  $Pe$  studied, is kinematic rather than dynamic: the effect of flow inertia is masked by the chaotic splitting/recombination mechanism whose influence inside the branches compensates for the low velocity and produces Nusselt numbers comparable to those in the higher-velocity zones where higher friction losses are encountered. As clearly seen on the local  $Nu$  plot, convective heat-transfer rates are highest in SAR-2, followed by SAR-1 and then 3D-Flow. The variation of the global Nusselt numbers with Péclet numbers is plotted in Fig. 9.

$Nu$  increases with  $Pe$  as the rate of advection increases in the flow for the same level of diffusion that plays an important role in the heat-transfer mode prevailing in the SAR configuration. However, the aim of the present work is to characterize forced convection and consequently the fluid diffusivity is kept constant at  $1.43 \times 10^{-7} \text{ m}^2 \text{ s}^{-1}$ . For the three configurations, the best enhancement is achieved in the intermediate Péclet number range, *i.e.* between  $10^3$  and  $10^5$ ; beyond this the relative increase diminishes and an inflection point in the curves can be detected around  $Pe = 10^6$ . It is in this zone also that the behavior of the three configurations is clearly distinct. On the one hand, for lower Péclet numbers, advection is too weak to accentuate the influence of the distinctive geometric features of each configuration. On the other hand, for high  $Pe$ , advection by the mean flow governs the transport phenomena and its effect masks that of chaotic splitting and recombination, accentuates the transverse secondary flow, and blunts the difference between the three heat exchangers. Heat transfer in the SAR-2 configuration is favored by its high ratio of number of splits/recombinations to the total developed length, together with the higher average velocity compared to SAR-1. This

latter geometry clearly induces higher transfer enhancement compared to the continuous 3D-Flow configuration: it is well established now that the chaotic effect of the SAR mechanism dominates that of the velocity and flow inertia, which is higher in 3D-Flow.

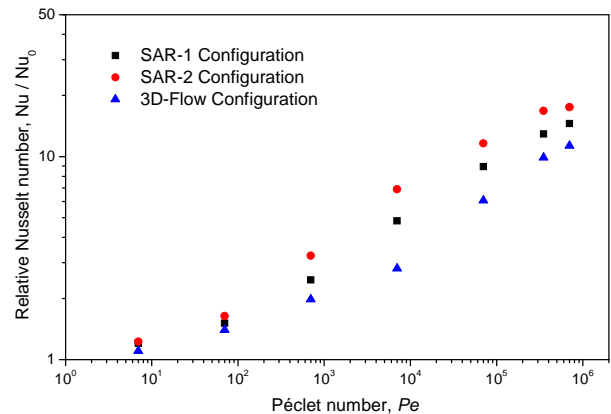


FIG. 9 RELATIVE NUSSLETT NUMBER VERSUS  $Pe$

The present study shows the interest of the SAR mechanism for mass and heat-transfer enhancement in creeping flows. In this deeply laminar zone, where the maximum Reynolds number value is 10, it was possible to enhance convective heat transfer as much as around 17-fold, a value comparable to that reported by Lasbet *et al.* [37] in a chaotic continuous-flow bent 3D geometry but for a much higher value of  $Re$ , *i.e.*  $Re = 200$ , where the secondary Dean flow accounts for the overall enhancement but with elevated energy expenditures. In order better to compare the global performance, the following section analyzes the head losses in the three configurations studied in the form of the normalized dimensionless friction factor.

### Friction losses

Figure 10 displays the variation of the normalized friction factor  $f/f_0$  with the inlet Péclet number whose range corresponds to Reynolds number values between  $10^{-4}$  and  $10^1$ . The friction factors are calculated from the total pressure drop (Eq. (10)) using the volume-averaged fluid velocity in each configuration. The model calculates the local static pressure by taking the zero pressure reference to be at the post-conditioner outlet as shown in Fig. 7(c). The ratio tends to increase with the rise of  $Pe$  values as the flow velocity increases and energy consumption becomes more important.

Major losses in the SAR-2 configuration exceed those in SAR-1 due to higher average velocities. SAR-1 incorporates more bends per unit but in SAR-2 the fluid undergoes a larger number of splits and recombinations. In fact, for this range of low Reynolds numbers, the major head loss coefficient well exceeds the minor coefficient of all singularities, and minor losses become negligible.

For low  $Pe$ , 3D-Flow consumes the least energy, but its consumption increases at a higher rate than the SAR configurations similarly owing to flow velocity considerations. More important than its evolution is the magnitude of the relative friction factor. For the heat-transfer enhancement achieved, one would expect the chaotic configurations to produce exponential increases in head losses, but this is not the case. For example, around  $Pe = 7 \times 10^5$ , compared to a plain channel, SAR-2 enhances Nusselt number by 17-fold with a mere 17% increase in the friction factor. The absence of flow blockage and the exploitation of the flow's own energy to enhance transport render the SAR configurations attractive in laminar flow applications where, as is expected, the global gain in the system energy balance exceeds that of other enhancement techniques as additional thermal power is transferred with moderate energy consumption.

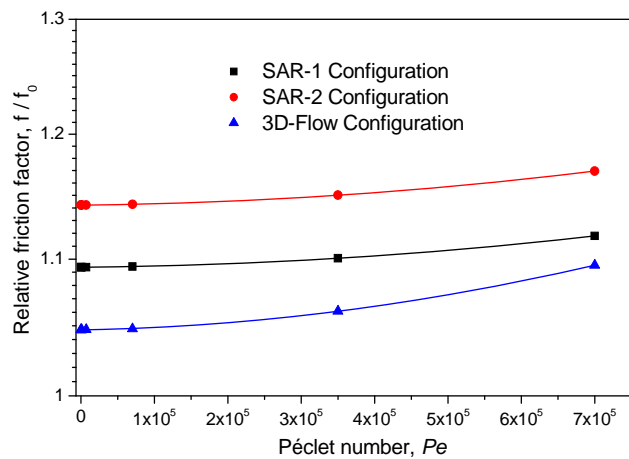


FIG. 10 RELATIVE FRICTION FACTOR VERSUS  $Pe$

### Performance evaluation

To explore the link between the thermal gain and the accompanying energy expenditures from a process-engineering perspective, we look further at the thermal enhancement factor introduced in Eq. (11). Figure 11 presents the variation of the thermal enhancement factor  $\eta$  in terms of  $Pe$ . This term quantifies the ratio of the modified geometry surface heat-transfer coefficient to that of a plain geometry at equal pumping power. As expected,  $\eta$  tends to increase with increasing  $Pe$ . The three configurations show similar heat transfer qualities for  $Pe < 100$ . More important on this plot is that, from an energy-efficiency perspective, SAR-2 retains the best position conveyed by the global  $Nu$  plot, although it produces higher head losses. The relative enhancement in  $Nu$  is more significant than the accompanying increase in the friction factor. At its best, for  $Pe = 35 \times 10^4$ , SAR-2 performs 28% better than SAR-1 and 65% better than 3D-Flow.

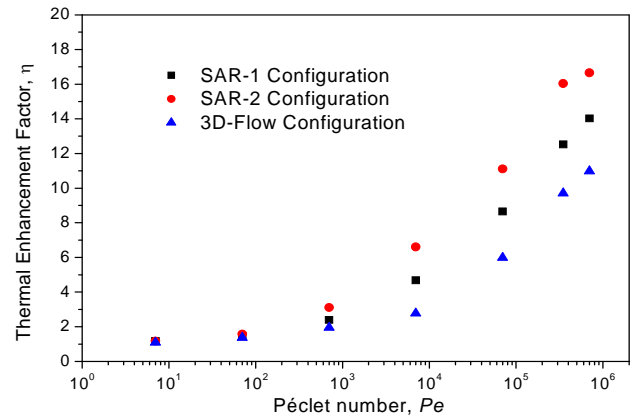


FIG. 11: THERMAL ENHANCEMENT FACTOR VERSUS  $Pe$

### CONCLUSION

Chaotic laminar flow and convective heat transfer in a three-dimensional continuous flow and two split-and-recombine (SAR) multifunctional heat exchangers/reactors are numerically investigated. Surface curvature and periodic flow deviations create spatial chaos within the three configurations. The SAR mechanism promotes the chaotic nature by exponentially increasing the interfacial area between the different fluid layers created by the consecutive diverging and converging zones of the geometries. Dynamic fluid particle trajectories and periodic variations in the local velocity field enhance mass transport. Heat transferred to the fluid particles through the constant-temperature walls is readily diffused throughout the entire section, and high convective heat-transfer rates contribute to the homogenization of the cross-sectional temperature distribution. Structural singularities produce even higher transfer rates, as reflected in abrupt localized increases in the surface Nusselt number.

Efficient heat transfer is achieved in deeply laminar creeping flow. Relative enhancements up to 1700% can be achieved over plain square channel flow, with a moderate increase in the pressure drop that does not exceed 17% in the worst case studied. The SAR-2 configuration exhibits the best performance, 28% better than the SAR-1 and 65% better than 3D-Flow. Increased splitting/recombination steps and better optimization of the velocity field distribution account for the higher efficiency. The chaotic configurations perform best for intermediate values of  $Pe$  between  $10^3$  and  $10^5$ , where the flow energy is most efficiently exploited to enhance mixing and heat transfer.

Scaled up from the microfluidic laboratory domain, the geometric characteristics of the optimized configurations permit them to handle flow rates characteristic of modern process industries. This type of reactor/heat exchanger can be widely used in pharmaceutical, cosmetic, chemical, and food industries where viscous, fragile, and reactive flows are frequently encountered.

## REFERENCES

- [1] Habchi, C., Russeil, S., Bougeard, D., Harion, J.-L., Lemenand, T., Della Valle, D., Peerhossaini, H., 2012, "Enhancing heat transfer in vortex generator-type multifunctional heat exchangers," *Appl. Therm. Eng.*, 38, pp. 12-25.
- [2] Lemenand, T., Dupont, P., Della Valle, D., Peerhossaini, H., 2005, "Turbulent mixing of two immiscible fluids," *J. Fluids Eng. Trans ASME*, 127, pp. 1132–1139.
- [3] Habchi, C., Lemenand, T., Della Valle, D., Peerhossaini, H., 2010, "Turbulent mixing and residence time distribution in novel multifunctional heat exchangers-reactors," *Chem. Eng. Process.*, 49, pp. 1066-1075.
- [4] Habchi, C., Lemenand, T., Della Valle, D., Peerhossaini, H., 2010, "Alternating mixing tabs in multifunctional heat exchanger-reactor," *Chem. Eng. Process.*, 49, pp. 653–661.
- [5] Ferrouillat, S., Tochon, P., Della Valle, D., Peerhossaini, H., 2006, "Open-loop thermal control of exothermal chemical reactions in multifunctional heat exchangers," *Int. J. Heat Mass Transfer*, 49, pp. 2479–2499.
- [6] Ghanem, A., Habchi, C., Lemenand, T., Della Valle, D., Peerhossaini, H., 2012, "Energy efficiency in process industry – High-efficiency vortex (HEV) multifunctional heat exchanger," *Renew. Energy*, in press, <http://dx.doi.org/10.1016/j.renene.2012.09.024>.
- [7] Mohand Kaci, H., Habchi, C., Lemenand, T., Della Valle, D., Peerhossaini, H., 2010, "Flow structure and heat transfer induced by embedded vorticity," *Int. J. Heat Mass Transfer*, 53, pp. 3575–3584.
- [8] Mohand Kaci, H., Lemenand, T., Della Valle, D., Peerhossaini, H., 2009, "Effects of embedded streamwise vorticity on turbulent mixing," *Chem. Eng. Process.*, 48, pp. 1457–1474.
- [9] Garcia, A., Vicente, P., Viedma, A., 2005, "Experimental study of heat transfer enhancement with wire coil inserts in laminar-transition-turbulent regimes at different Prandtl numbers," *Int. J. Heat Mass Trans.*, 48, pp. 4640–4651.
- [10] Chemineer, Kenics: Static Mixing Technology, Chemineer Inc., Bulletin 800 (commercial documentation), Dayton, OH, 1998.
- [11] Schwarze, R., Klostermann, J., Brücker, C., 2008, "Experimental and numerical investigations of a turbulent round jet into a cavity," *Int. J. Heat Fluid Flow*, 29, pp. 1258–1267.
- [12] Habchi, C., Ouarets, S., Lemenand, T., Della Valle, D., Bellettre, J., Peerhossaini, H., 2009, "Influence of viscosity ratio on droplets formation in a chaotic advection flow," *Int. J. Chem. Reactor Eng.*, 7, A50, pp. 1–14.
- [13] Momayez, L., Dupont, P., Peerhossaini, H., 2004, "Some unexpected effects of wavelength and perturbation strength on heat transfer enhancement by Görtler instability," *Int. J. Heat Mass Transfer*, 47, pp. 3783–3795.
- [14] Lemenand, T., Peerhossaini, H., 2002, "A thermal model for prediction of the Nusselt number in a pipe with chaotic flow," *Appl. Therm. Eng.*, 22 (15), pp. 1717–1730.
- [15] Habchi, C., Lemenand, T., Della Valle, D., Peerhossaini, H., 2009, "Liquid-liquid dispersion in a chaotic advection flow," *Int. J. Multiphase Flow*, 35, pp. 485-497.
- [16] Mokrani, A., Castelain, C., Peerhossaini, H., 1998, "The effect of chaotic advection on heat transfer," *Int. J. Heat Mass Transfer*, 40, pp. 3089–3104.
- [17] Acharya, N., Sen, M., Chang, H.C., 1992, "Heat transfer enhancement in coiled tubes by chaotic advection," *Int. J. Heat Mass Transfer*, 35, pp. 2475–2489.
- [18] Lichtenberg, M. A., Lieberman, A. J., 1992, "Regular and Chaotic Dynamics," Springer, New York, USA.
- [19] Ottino, J. M., 1989, "The Kinematics of Mixing: Stretching, Chaos and Transport," Cambridge University Press, New York.
- [20] Wiggins, S., Ottino, J. M., 2004, "Foundations of chaotic mixing," *Philos. Trans. R. Soc. London (A)*, 362, p. 937.
- [21] Gray, B. L., Jaeggi, D., Mourlas, N. J., Van Drieënhuizen, B. P., Williams, K. R., Maluf, N. I., Kovacs, G. T. A., 1999, "Novel interconnection technologies for integrated microfluidic systems," *Sensors Actuators*, 77, pp. 57–65.
- [22] Chen, H., Meiners, J. C., 2004, "Topologic mixing on a microfluidic chip," *Appl. Phys. Lett.*, 84(12), pp. 2193–2195.
- [23] Carrière, P., 2007, "On a three-dimensional implementation of the baker's transformation," *Physics of Fluids*, 19 (11), no. 118110.
- [24] Schönfeld, F., Hessel, V., Hofmann, C., 2004, "An optimised split-and-recombine micro-mixer with uniform 'chaotic' mixing," *Lab Chip*, 4, pp. 65–69.
- [25] Xia, H. M., Wan, S. Y. M., Shu, C., Chew, Y. T., 2005, "Chaotic micromixers using two-layer crossing channels to exhibit fast mixing at low Reynolds numbers," *Lab Chip*, 5, pp. 748–755.
- [26] Ohkawa, K., Nakamoto, T., Izuka, Y., Hirata, Y., Inoue, Y., 2008, "Flow and mixing characteristics of  $\sigma$ -type plate static mixer with splitting and inverse recombination," *Chem. Eng. Res. Des.*, 86, pp. 1447–1453.
- [27] Lester, D. R., Rudman, M., Metcalfe, G., 2009, "Low Reynolds number scalar transport enhancement in viscous and non-Newtonian fluids," *Int. J. Heat Mass Trans.*, 52, pp. 655–664.
- [28] Peerhossaini, H., Bahri, F. 1998, "On the spectral distribution of the modes in nonlinear Görtler instability," *Experimental Thermal and Fluid Science*, (16) pp. 195-208.
- [29] Toledo, R. T., 1999, *Fundamentals of Food Process Engineering*, 2d ed., Chapman & Hall, New York.
- [30] Metcalfe, G., Lester, D., 2009, "Mixing and heat transfer of highly viscous food products with a continuous chaotic duct flow," *J. Food Eng.*, 95, pp. 21–29.
- [31] Warming, R. F., Beam, R. M., 1975, "Upwind second-order difference schemes and applications in unsteady aerodynamic flows," *Proc. AIAA 2nd Computational Fluid Dynamics Conference*, Hartford, CT, pp. 17–28.
- [32] Barth, J. T., Jespersen, D., 1989, "The design and application of upwind schemes on unstructured meshes," *Technical Report AIAA-89-0366*, AIAA 27th Aerospace Sciences Meeting, Reno, Nevada.
- [33] Vandoormaal, J. P., Raithby, G. D., 1984, "Enhancements of the SIMPLE method for predicting incompressible fluid flows," *Numer. Heat Tr.*, 7, pp. 147–163.
- [34] Incropera, F., Dewitt, P. D., 2006, *Introduction to Heat Transfer*, 5th ed., John Wiley & Sons Inc.
- [35] Dean, W. R., 1927, "Note on the motion of fluid in a curved pipe," *Philos. Mag.*, 4, pp. 208–223.
- [36] Lasbet, Y., Auvity, B., Castelain, C., Peerhossaini, H., 2006, "A chaotic heat-exchanger for PEMFC cooling applications," *J. Power Sources*, 156, pp. 114–118.